Available online at www.sciencedirect.com

ScienceDirect

Acta Materialia 79 (2014) 168–180

Acta MATERIALIA

www.elsevier.com/locate/actamat

3-D microstructural model of freckle formation validated using in situ experiments

S. Karagadde [a,b], L. Yuan [c], N. Shevchenko [d], S. Eckert [d], P.D. Lee [a,b,*]

[a] Manchester X-ray Imaging Facility, University of Manchester, Oxford Road, Manchester M13 9PL, UK
[b] Research Complex at Harwell, Rutherford Appleton Laboratory, Harwell OX11 0FA, UK
[c] GE Global Research, Niskayuna, NY 12309, USA
[d] Helmholtz-Zentrum Dresden-Rossendorf, Institute of Fluid Dynamics, PO Box 510119, 01314 Dresden, Germany

Received 13 March 2014; received in revised form 1 July 2014; accepted 2 July 2014

Abstract

A 3-D model of freckle (solute channel) formation at a microstructural level was coupled with in situ X-ray radiography to investigate the mechanisms of freckle initiation and growth. The model predictions for solute partitioning, diffusion and convection were validated via in situ X-ray radiographic measurements in Ga–25 wt.% In alloy, showing good agreement. Other key features, such as freckle channel width and critical Rayleigh number, also correlated well. The validated model was used to investigate freckle formation under a range of solidification conditions. Two distinct stages of freckle onset were observed, identified via the dendrite tip growth and solute profiles. The first stage corresponds to lower flow velocities with large fluctuations; in the second stage the velocities stabilize, with established recirculating flows forming solute channels. The influence of imperfections in dendritic morphology, such as grain boundaries and primary spacing variations, on the critical Rayleigh number was studied. It was found that that these features initiate freckles. Non-intuitively, converging grain boundaries were observed to have the greatest propensity for freckle formation. The resulting new insights on solute plume formation impact a range of phenomena from single-crystal superalloys to magma flows.

Keywords: Freckles; Microstructure; Solidification defects; Solute transport; Chimney formation

1. Introduction

Convection due to thermal and compositional variation can cause the formation of preferential flow channels (termed freckles, solute channels, chimneys or solute fingering), which can be found in a wide range of situations ranging from naturally occurring magma reservoirs [1,2] to man-made cast alloy components [3,4]. Such systems, which typically involve two or more components with different densities and phases, often exhibit natural convection due to density variations in the liquid caused by thermal and compositional gradients. This convection then draws liquid from the surroundings, forming a stable chimney [5]. In a casting, it may result in narrow but elongated solute-rich regions which solidify during the final stage of solidification. These channels are typically formed in the interdendritic regions upon localized segregation and enrichment. Such regions, typically consisting of grain boundaries and disoriented crystals, are manifested as freckle defects or A-segregates [6–10].

Nickel-based superalloys, employed in the manufacturing of single-crystal gas turbine blades, are highly prone to freckles [11–14]. Such channel segregates are also observed in several steel grades, particularly in the centreline regions of continuous cast slabs [15]. Moreover,

* Corresponding author at: Manchester X-ray Imaging Facility, University of Manchester, Oxford Road, Manchester M13 9PL, UK.
E-mail addresses: peter.lee@manchester.ac.uk, p.d.lee@ic.ac.uk (P.D. Lee).

http://dx.doi.org/10.1016/j.actamat.2014.07.002
1359-6454/

turbine blades typically involve very expensive alloying elements and are designed to operate at temperatures close to 85% of their melting point, thus requiring them to be defect-free and highly efficient. These defects result in an enormous increase in the rate of scrappage (~49% loss), incurring increased production costs and energy consumption, and thus need to be better understood in order to improve the manufacturing processes.

A number of experimental and numerical studies have been conducted to understand the occurrence and evolution of these defects. Most of the experimental studies have been ex situ and macroscopic [3,14,16,17], mainly due to the complexities involved with handling Ni-based alloys at high temperatures. Recently, an in situ radiographic technique to study freckle formation was developed by Eckert and co-workers [7,18,19]. A Ga–In alloy was used due for two key properties: it is prone to freckle formation; and it has a melting point near room temperature for easy handling. Using this technique, Shevchenko et al. [18] reported formation of stable chimneys at several solidification conditions, and successfully captured the solute distribution and flow velocities to quantify the defects. In this paper we use this technique to validate the model simulations.

Numerical models have been developed to predict the phenomena of solidification and freckle formation [8,13,20,21]. Using mathematical criterion models, the occurrence of freckle defects in a casting can be predicted based on solidification conditions. Such models are typically based on the Rayleigh number (Ra), which gives an estimate of the strength of natural convection during solidification [9,14]. A wide range of phenomenological models have also been developed but are mainly macroscopic, simulating macrosegregation in the bulk domain during solidification [8,22–25]. This is conventionally performed by coupling with fluid flow to identify regimes of solute accumulation and the resulting transport through natural convection. However, such models provide very little information regarding the microscopic processes such as solute accumulation and interdendritic fluid flow in the mushy region.

Microstructural 2-D models [13,26–30] have demonstrated such dendritic solidification in the presence of natural convection. However, these models are not applicable for freckle channel formation studies as 3-D analysis is essential to capture the interdendritic flow, as demonstrated by Yuan and Lee [10]. These authors performed the first direct simulations of freckle formation in Pb–Sn alloys using the open source microstructural solidification code μMatIC [31–34], proposing three mechanisms that lead to initiation and formation of freckles, namely: (i) dendrite remelting (ii) dendrite overgrowth and (iii) dendrite deflection. However, the model was only validated via the critical Rayleigh number predictions.

In this work, we extend μMatIC and validate it by direct comparison with in situ radiographic quantification of dendritic structures, solute partitioning and flow velocities. This validated model was then applied to investigate the freckle characteristics and the effects of microstructural defects, such as grain boundaries (both converging and diverging) and variations in primary arm spacing, on freckle initiation.

2. Model description and the experimental setup

2.1. Mathematical modeling

The microstructure solidification code μMatIC [35] simulates dendrite morphology, solute partitioning and diffusion with microsegregation under both forced and natural convection during solidification processes. The model assumes that the liquid is incompressible and Newtonian. The effect of shrinkage due to the density difference between solid and liquid phases is neglected. The growth of the solidifying interface is obtained by the equilibrium thermal and solute balance at the interface using established relationships. The entire framework follows the approach described in Refs. [10,31,33]. The governing equations are given as follows.

2.1.1. Governing equations

The mass and momentum conservation are imposed by using the Navier–Stokes equation for incompressible flow. Buoyancy source terms are incorporated to represent natural convection arising from thermal and solute gradients:

$$\nabla \cdot (f_l \vec{\mathbf{u}}) = 0 \tag{1}$$

$$\frac{\partial}{\partial t}(f_l \rho \vec{\mathbf{u}}) + \nabla \cdot (f_l \rho \vec{\mathbf{u}}\vec{\mathbf{u}}) - \nabla \cdot [\mu \nabla (f_l \vec{\mathbf{u}})] = -\nabla (f_l P) + S_{\mathrm{F}}, \tag{2}$$

where $\vec{\mathbf{u}}$ is the velocity vector in the liquid, f_l is the mass fraction of the liquid phase (denoted by the subscript l), $\boldsymbol{\rho}$ is the density of the liquid phase, P is the pressure, $\boldsymbol{\mu}$ is the viscosity, and $\mathbf{S}_{\mathrm{F}}$ is the source accounting for the thermal and compositional dependence of the liquid density, and is given by the following equation:

$$S_{\mathrm{F}} = \rho_0 \mathbf{g} f_l (1 + \beta_T (T - T_{\mathrm{ref}}) + \beta_C (C - C_{\mathrm{ref}})), \tag{3}$$

where ρ_0 is the density calculated at the bulk composition, $\mathbf{g}$ is the gravitational acceleration, β_T and β_C are thermal and compositional expansion coefficients, and T and C are the temperature and concentration variables, with the subscript "ref" denoting a reference state (in this study, the initial condition is taken for this state).

The heat (energy) and solute conservation relations are given by:

$$\frac{\partial T}{\partial t} + f_l \vec{\mathbf{u}} \cdot \nabla T = \frac{\eta}{\rho c_p} \nabla^2 T - \frac{L}{c_p} \frac{\partial f_l}{\partial t} \tag{4}$$

$$\frac{\partial C_e}{\partial t} + \vec{\mathbf{u}} \cdot \nabla C_l = \nabla \cdot (D_e \nabla C_l), \tag{5}$$

where c_p is the specific heat, η is the thermal conductivity, L is the latent heat, and C_s and C_l are the average solute concentrations of the solid and liquid. The terms C_e and D_e are the averages calculated using their respective values in liquid and solid phases, i.e. $C_e = f_l C_l + f_s C_s$ and $D_e = f_l D_l + k f_s D_s$. Here, D_l and D_s are solute diffusion coefficients in the liquid and solid, respectively, and k is the partitioning coefficient. This allows the solute diffusion equation (Eq. (5)) to be adapted to the entire domain, including the liquid, solid and mushy regions. The rate of change of the solid fraction (f_s) at the solid–liquid interface is obtained by the following relation [20,33]:

$$\frac{\partial f_s}{\partial t} = \frac{1}{C_l(1-k)}\left[-\frac{\partial C_e}{\partial t} + [1-(1-k)f_s]\frac{\partial C_l}{\partial t}\right]. \tag{6}$$

The governing thermal and species transport equations are solved on the regular spatial grid. The flow velocity through the mushy zone is proportionally dampened using the values for the solid fraction [10]. The solidifying front is advanced when a positive change in the solid fraction is encountered, where a negative change implies remelting. This work utilizes the modified decentered square/octahedron algorithm described in Wang et al. [33] to impose anisotropy of the interfacial energy at the solid–liquid interface. The significant advantage of this methodology over other numerical methods, such as phase field or level set, is that a coarser grid (by an order of magnitude) can be used, thus achieving considerable reduction in computing effort. However, this is prone to cause errors in the values of tip undercooling, which requires high resolution of interfacial grids. For a typical case, this error was found to be of the order of 5% [33]. This approach has been validated against experiments in terms of solute diffusion at the interface, primary dendritic arm spacing and the columnar-to-equiaxed transition [33,34]. Such an approach allows one to incorporate fluid flow in the model to directly calculate complex, multigrain solidification microstructures and the subsequent effect of natural and forced convection.

2.1.2. Initial and boundary conditions

A schematic of the domain and boundary conditions used in the current study is shown in Fig. 1. The phase diagram for the Ga–In binary system is represented in Fig. 2 [36]. The simulation parameters and conditions are listed in Table 1. Fixed nuclei were placed at the bottom to initiate dendrite growth, using the primary arm spacing calculated from the analytical relation proposed by Hunt and Lu [37]. The dimensionless spacing is given by the relation $\lambda_1' = 0.078\, V'^{(a-0.75)}(V'-G')^{0.75}\, G'^{-0.6028}$, where a is a constant, and V' and G' are non-dimensional values of speed and thermal gradient, respectively [37]. This was calculated to be 274 μm for $G = 1\ \mathrm{K\ mm^{-1}}$ and $R = 8\ \mu\mathrm{m\ s^{-1}}$ (Table 1). The crystallographic orientation was set to be same for all the seeds. Although the simulation domain is smaller than that of the experimental study, measured values of the thermal gradient and pulling velocity were imposed. Periodic boundary conditions were used on the thin side surfaces and a zero derivative boundary condition was applied to the top, bottom, front and back surfaces for velocities and solute concentration.

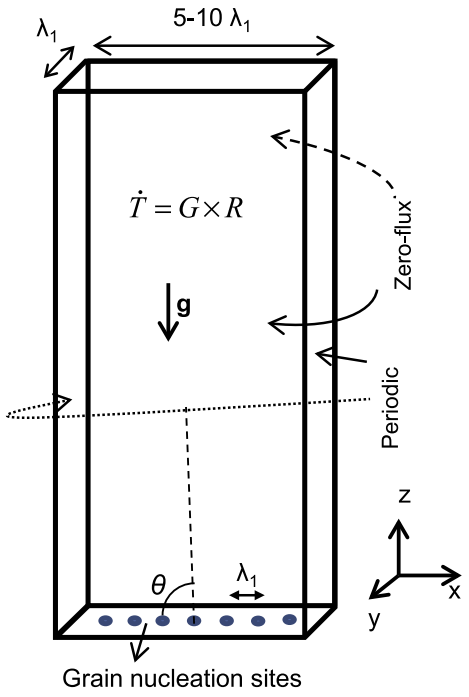

Fig. 1. Schematic of the computational domain and boundary conditions.

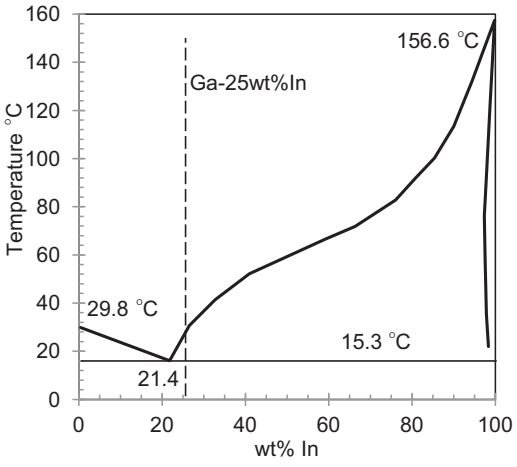

Fig. 2. Phase diagram of Ga–In binary alloy system, with the dashed line showing the alloy used in the present study [36].

2.2. Estimation of the Rayleigh number (Ra)

The Rayleigh number is the dimensionless quantity typically used for describing buoyancy driven flows. It compares the contributions to heat or mass transfer arising from diffusion and convection, respectively. In

Table 1
Thermophysical property values used in the simulation.

Property	Variable	Value	Unit	Reference
Partitioning coefficient	k	0.05	–	Estimated
Liquidus slope	m	1.8	K wt.%$^{-1}$	[38]
Melting point of Ga	T_m	302.77	K	[39]
Liquidus temperature	$T_{liquidus}$	298	K	[18]
Latent heat	L	4.2×10^8	J m^{-3}	[39]
Specific heat	c_p	380.4	J kg^{-1} K^{-1}	[39]
Eutectic temperature	T_{eut}	288.3	K	[38]
Eutectic concentration	C_{eut}	21.4	wt.% In	[38]
Kinematic viscosity	v	3.28×10^{-7}	m^2 s^{-1}	[40]
Solute expansion coefficient	β_c	1.66×10^{-3}	wt.%$^{-1}$	[39]
Thermal expansion coefficient	β_T	1×10^{-4}	K^{-1}	[39]
Thermal diffusivity	α	4.918×10^{-3}	m^2 s^{-1}	[39]
Solute diffusivity in liquid	D_L	2×10^{-9}	m^2 s^{-1}	[41]
Solute diffusivity in solid	D_S	1×10^{-12}	m^2 s^{-1}	[41]
Thermal gradient	G	1	K mm^{-1}	[18]
Solidification velocity	R	8	μm s^{-1}	[18]
Initial temperature	T_{init}	300	K	–
Orientation angle	$90 - \theta$	2	deg	–
PDAS (for given G and R)	λ_1	274	μm	[37]
Ga concentration	C_{init}	75	wt.%	–

solidification processes, such a criterion can be used to predict the occurrence of freckles [9,13,14]:

$$Ra_h = \frac{gKh}{\alpha v}\left(\frac{\Delta\rho}{\rho_0}\right) \tag{7}$$

where h is the characteristic length scale, K is the mean permeability of the mushy zone, α is the thermal diffusivity, v is the kinematic viscosity, and the term $\frac{\Delta\rho}{\rho_0}$ is the density change due to thermal and/or compositional variation. In this work, length scale (L), permeability (K) and density inversion $\frac{\Delta\rho}{\rho_0}$ are evaluated following Ramirez et al. [9]. For a given (experimental) casting speed R and a primary arm spacing λ_1, the length scale is estimated by the relation $h = \alpha/R$ and the permeability using the following empirical relation:

$$K = 0.074 \cdot \lambda_1^2 \cdot \left(-\ln \overline{f_s} - 1.49 + 2\overline{f_s} - 0.5\overline{f_s}^2\right) \tag{8}$$

The maximum value of the Ra (as a function of solid fraction) across the mushy zone is chosen to evaluate the strength of convection, which is then correlated to the occurrence of freckle defects.

2.3. Experimental setup

The experimental data used for validation are based on in situ solidification of Ga–25 wt.% In alloy in a Hele–Shaw cell $25 \times 35 \times 0.15$ mm^3 in size [18]. The X-ray observation was performed over a 22.5 mm × 30 mm rectangular window. The Hele–Shaw cell was cooled at the bottom by means of a Peltier cooler at ~0.01 K s^{-1}. An electrical heater was installed at the upper part of the solidification cell. Different heating powers ranging from 0 to 1.7 W were applied to control thermal gradient over the domain. A microfocus X-ray tube (Phoenix XS225D-OEM) was used to perform the radioscopy. Solute concentration distribution and flow velocities were derived from the captured images using the information from brightness variation and the optical flow approach, respectively [18,19]. This novel experiment provides an ideal case for validating numerical models by allowing visual tracking of the dynamics of microstructure/freckle formation. Moreover, the setup of a solidification cell with a thin gap provides a much simpler domain for numerical solutions.

The procedure for obtaining compositional distribution from the X-ray radiography images is briefly described here. The X-ray radioscopy delivers a 2-D projection of the local density in the slit container corresponding to the distribution of the relative brightness P in the acquired images. The 2-D scalar field P is defined as follows:

$$P = \frac{I - I_{dark}}{I_0 - I_{dark}} \tag{9}$$

where I_0 and I denote the intensities at the respective pixel location obtained from the initial state and from the consecutively recorded images, respectively, and I_{dark} is the camera's dark current signal. The relative brightness P allows for an assessment of the local composition inside the liquid phase. The calibration for measuring the composition was performed by using area reference measurements of a cell filled with Ga liquid. Further details on the technique can be found in Refs. [18,42].

Secondly, the analysis of the flow field follows the optical flow approach proposed by Horn and Schunck [43]. The details of the approach and results concerning the flow structures in the melt can be found in Ref. [7]. This algorithm to determine the optical flow from the X-ray images delivers reliable information on the velocity field in regions where sufficiently large brightness gradients occur. The

flow field is evaluated by monitoring the temporal variations of characteristic brightness patterns in the liquid phase. Other values, such as tip velocity and tip solute concentration, are obtained by measuring the height of a 5 pixel × 5 pixel window just ahead of the interface representing the tip of the dendrite.

3. Results and discussion

The model is first validated against the in situ experiments. The stages leading up to, and during, freckle formation are then quantified, including characterizing dendrite tip growth rates and solute profiles. Finally, the influences of irregularities in the dendrite arm spacing and grain boundary orientation upon freckle formation are investigated.

3.1. Model validation

Exact experimental values of solidification conditions were imposed in the numerical study. However, a smaller simulation domain ($4 \times 10 \times 0.15\ mm^3$, grid size 10 μm) than the experimental container ($25 \times 35 \times 0.15\ mm^3$) was used for computational efficiency. The numerical domain was selected as a trade-off of sufficient size to capture freckle formation against computational speed (~1 week on a desktop PC). The values of the thermophysical properties used in the simulation are listed in Table 1.

Fig. 3 shows a typical simulation of dendritic solidification, with the gradual formation of a solute channel leading to freckle formation. Note, in Fig. 3d, four dendrites are marked a–d and three interdendritic regions are marked 1–3, to identify and explain several features in the following discussion. The spacing between primary dendritic arms was obtained from the Hunt and Lu model [37] and is also found to match with the experimental result [18]. During the early stages, the front remains predominantly flat, but, due to solute partitioning at the dendrite–liquid interface, Ga is rejected from the α-dendrites (kC_l) and its concentration gradually increases in the mushy region. The Ga is lighter than In, and therefore natural convection is initiated and the interdendritic liquid flows upwards (Fig. 3b), increasing the plume velocity from ~1 μm s^{-1} to 30 μm s^{-1}. This upward flow of Ga-enriched liquid causes the secondary arms to remelt and inhibits any further local dendrite growth. As shown in Fig. 3d, the secondary dendrite arms for the dendrite "b" on the left-hand side (Ga enriched) are much shorter than on the right-hand side. In addition, a reciprocal downward flow (recirculation) occurs into the neighboring interdendritic spaces (labeled 1), transporting enriched liquid and making neighboring dendrites ("a" and "b") grow faster (Fig. 3c). Note that the length scale of the initial convection cells as seen from the vectors shown in Fig. 3b–d is comparable to the primary dendrite arm spacing (PDAS). This indicates that the freckle formation behavior is primarily microscopic as proposed by Yuan and Lee [10].

The model and experimental results are compared in Fig. 4. The predicted contours of Ga concentration (Fig. 4a) and freckle channel width (400 μm in both) match closely with the values obtained from the experiment (Fig. 4b). The fluid flow pattern and velocities were also found to compare well. Fig. 5 shows the snapshots from the experiment (Fig. 5a) and numerical simulation (Fig. 5b), highlighting the flow velocity vectors and their pattern in a representative region. The optical velocity calculation method is very appropriate for plumes with large Ga concentration variation. However, slight differences between the numerical and experimental results are observed, which are primarily due to the difference in the height of the solidification cells. Note that the optical flow approach does not resolve the lower magnitude flow vectors (<20 μm s^{-1}) due to weak concentration gradients.

3.2. Effect of solidification conditions on freckle formation

Freckle susceptibility has been found to decrease with *Ra* number [9,13]. The *Ra* number can be varied by altering the thermal gradient and solidification velocity, allowing the dependence of freckle formation to be evaluated for Ga–In alloys. Both thermal gradient and solidification velocity vary during casting, providing direct insights into key metallurgical processes. Therefore, simulations were performed for a range of solidification conditions as given in Table 2, and with comparable Rayleigh number (using Eq. (7)) to the experiments of Shevchenko et al. [18]. When calculating *Ra* in this table, the permeability *K* (Eq. (8)) and density inversion $\Delta\rho/\rho_0$ are calculated from the relations described in Ramirez et al. [9].

In many prior ex situ experiments, there is a critical *Ra* number below which freckles do not occur [13]. In the experimental work, as shown in cases 1 and 3 of Table 2, freckles were found at both solidification conditions. The model was run for both these cases and a range of higher cooling rates (lower *Ra* values). The model predicted freckle formation for these *Ra* numbers, approximately 350 and 160. However, when the *Ra* number was reduced (via cooling rate) just below the critical value, a gradual transition towards non-existence of freckle channels was observed. This transition was roughly predicted when channels appear to form but were eventually suppressed. An example of such a transition (corresponding to case 5 from Table 2) is shown in Fig. 6a, at 800 s and $Ra = 143$ (case 5), with slightly enhanced channels shown in black circles. As faster solidification velocities were imposed, *Ra* was further reduced and no evidence of freckle formation was noticed (e.g. Fig. 6b at 600 s for $Ra = 129$, case 6). The model, therefore, predicts a critical *Ra* value of ~150 for this alloy. These predictions match well with the experimental observations, where many fewer freckles were seen in case 3, when the *Ra* number was just above the critical value (150).

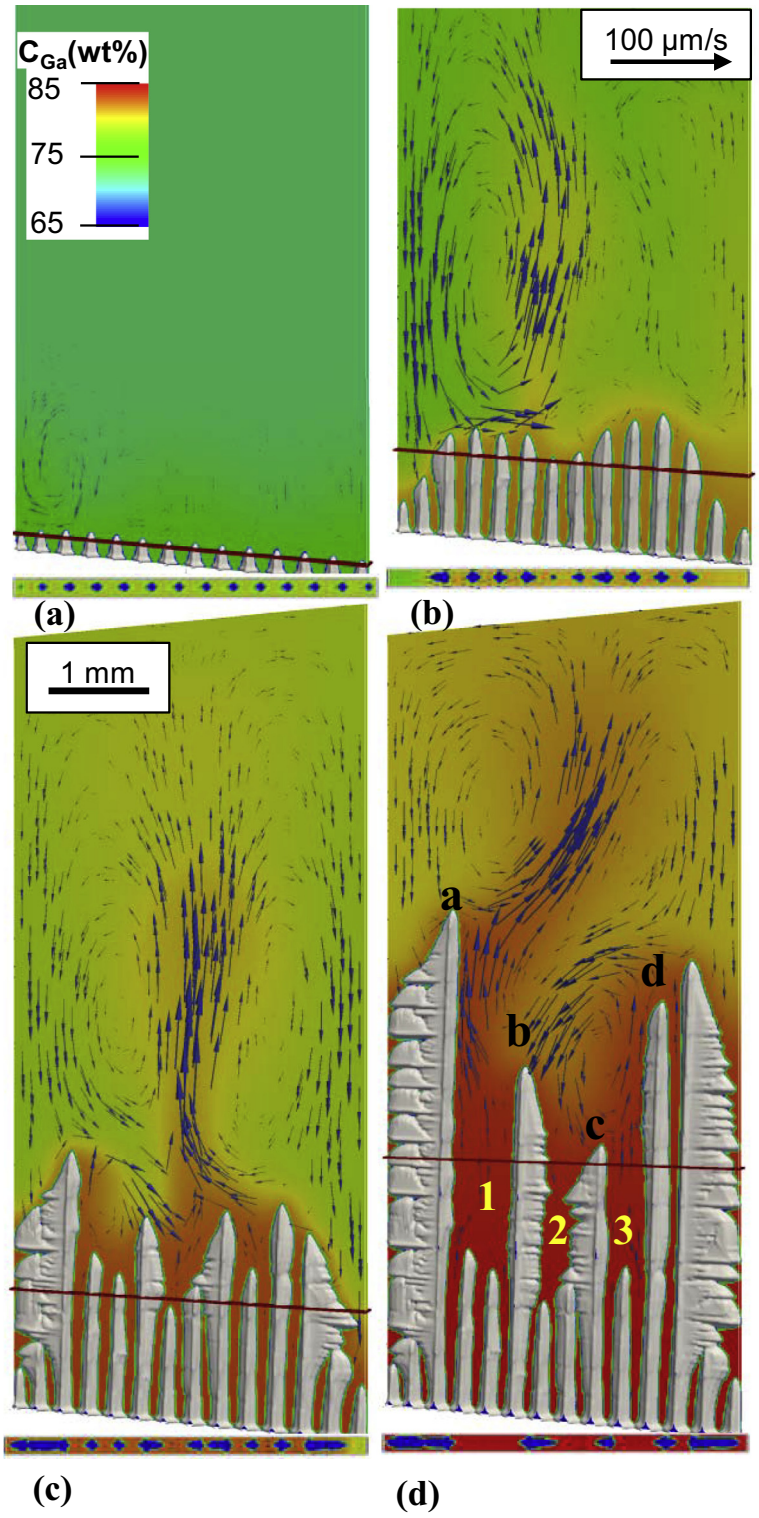

Fig. 3. 3-D simulation of freckle initiation and sustained growth showing solute field and flow vectors on x–z (top) and x–y (bottom), at t = (a) 72 s, (b) 397 s, (c) 685 s, (d) 1260 s.

3.3. Dendrite tip velocity and solute concentration

It is well known that the tip velocity is significantly altered in presence of convection due to the influence it has on the solute boundary layer [44]. The tip velocity, or growth rate, depends on the local undercooling, which depends upon both temperature and the solute level. These, in turn, are altered by any melt flow, as it can advect the solute away, or to the tip. Freckle formation has conventionally been investigated at a macroscopic level, and the

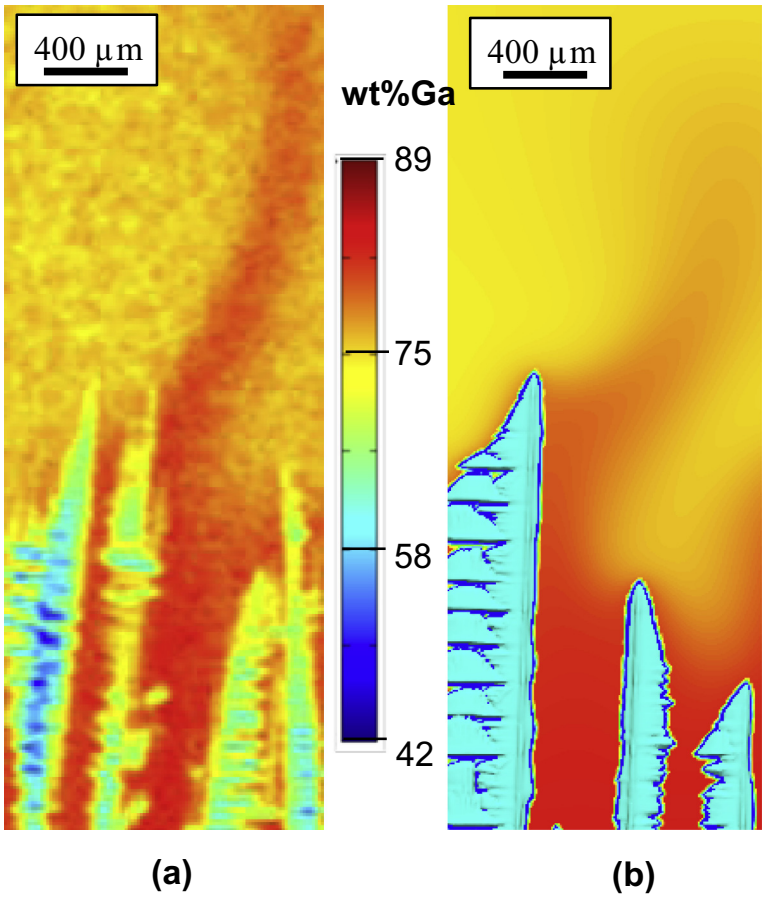

Fig. 4. Comparison of (a) experiment and (b) numerical simulation, showing a similar solute plume.

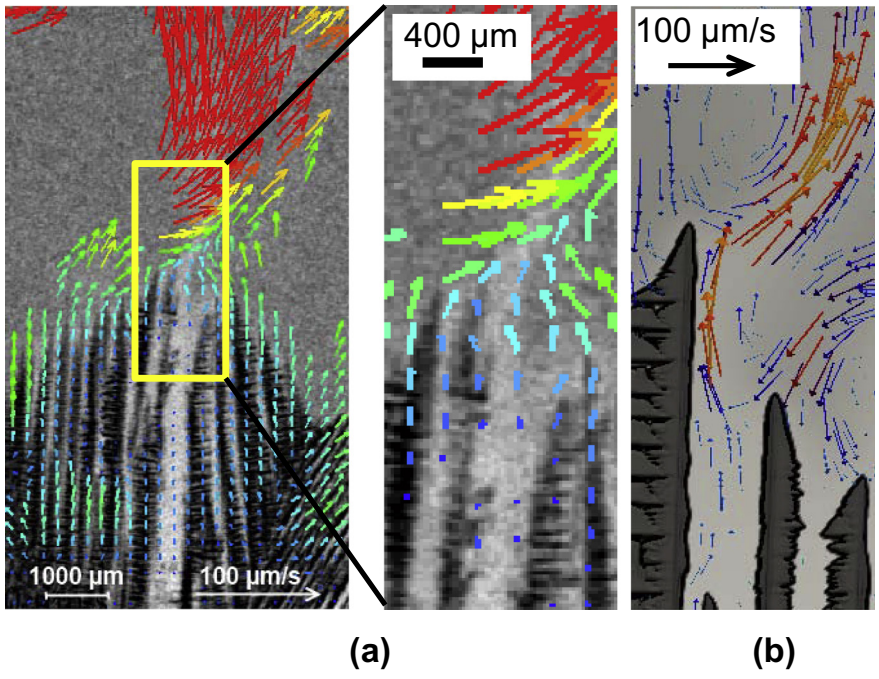

Fig. 5. Comparison of (a) experimental flow vectors obtained using the optical flow velocimetry (with a magnified view), and (b) simulated velocities.

Table 2
Comparison of experiment and model prediction for a range of solidification conditions.

Case	Solidification condition		Simulation		Experiment [18]	
	G (K mm^{-1})	R (μm s^{-1})	*Ra*	Freckle susceptibility?	*Ra*	Freckle susceptibility?
1	1	8	351	Y	335	Y
2	2	10	171	Y	–	–
3	1	15	162	Y	158	Y
4	2	15	152	Y	–	–
5	4	20	143	N	–	–
6	10	30	129	N	–	–
7	10	40	100	N	–	–

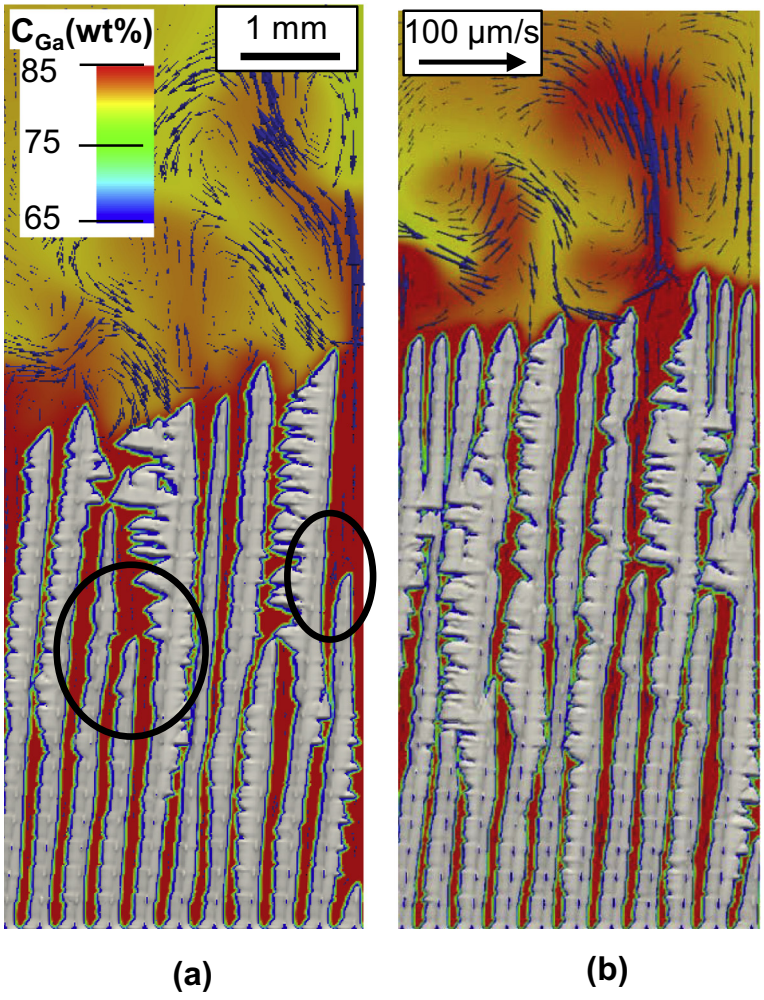

Fig. 6. Suppressed channel formation at lower *Ra*: (a) transition-like (weak freckle channels shown in black circles) behavior observed at $Ra = 143$ (case 5 of Table 2); and (b) no-freckle channels for $Ra = 129$ (case 6 of Table 2).

impact on tip velocity has not been documented. In this study, dendrite tip velocities adjacent to freckle channels are plotted to provide further insights into freckle phenomena. As solute channels form, both dendrite overgrowth and deflection [10] were observed (Fig. 3), helping form distinct freckle channels. The tip velocities for four of the dendrites (as marked in Fig. 3d) are compared in Fig. 7a. Two distinct stages in the tip velocity can be identified in Fig. 7a, corresponding to the two key stages that the model predicts during freckle formation:

Stage I—freckle initiation: partitioned solute forms localized density inversions that cause initially small flows and recirculation cells. These cells then quickly grow, compete with each other, advecting solute with them.

Stage II—freckle stabilization and sustained growth: after a period of time, one convection cell dominates, often due to its having remelted the secondary dendrites, and subsequently stabilizing the chimney flow.

Stage I is clearly visible via the strong fluctuations in the tip growth velocities during the first 700 s (Fig. 7),

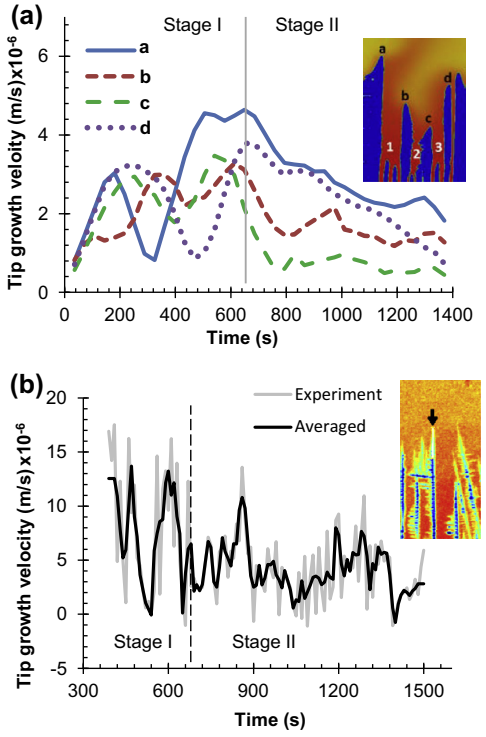

Fig. 7. (a) Dendrite tip velocity for four dendrites (labeled in Fig. 3d) vs. simulation time showing two distinct stages of growth behavior. (b) Experimentally measured velocity (raw and averaged).

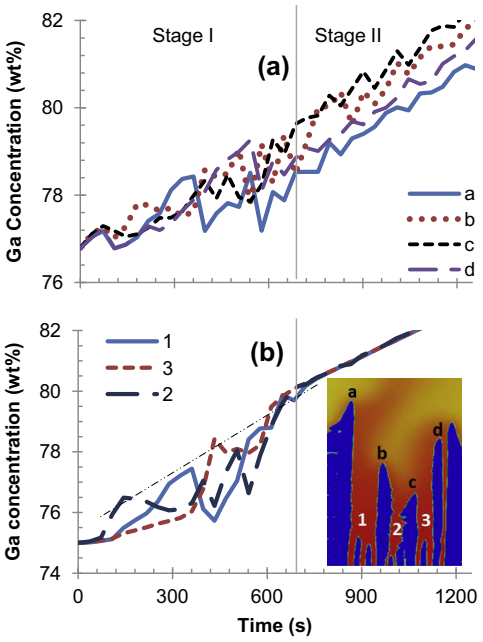

Fig. 8. Solute (Ga) concentration vs. time (a) from ahead of the dendrite tips (marked a–d) that are adjacent to the freckle channels, and (b) from freckle-like channels (marked 1–3 in the inset).

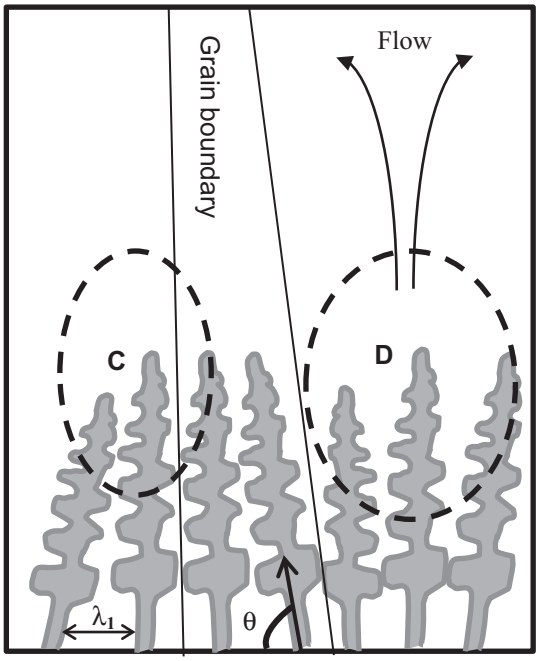

Fig. 9. Schematic representation of a grain boundary defect showing converging (C) and diverging (D) primary dendrites with a spacing of λ_1 and orientation angle θ.

corresponding to the fluctuations in flow as the convection cells form and compete with each other in the melt. These fluctuations cause the solute layer ahead of the tip to fluctuate between being enriched and depleted, slowing and accelerating the tip growth, respectively. At 700 s, a stable plume is established, as seen in Fig. 3c and d. This brings Ga-enriched interdendritic liquid upwards, broadening the solute field around tips "b" and "c". This reduces the tip undercooling and the tip growth velocities. However, the upward flow must be fed by an equivalent downward flow, which brings Ga-depleted fluid to the neighboring tips "a" and "d", resulting in increased undercooling and tip velocity relative to those of "b" and "d".

Fig. 7b shows the variation of tip growth velocity over time, plotted from the experimental data corresponding to similar solidification conditions. The freckle channel and the dendrite under consideration are also shown in the inset of the figure. If the plots in Fig. 7a and b are carefully compared, the order and nature of fluctuations are reasonably similar, confirming the correctness of the model. Furthermore, the experimental plot qualitatively depicts the two stages of freckle formation as predicted by the model (Fig. 7a). The experimental tip velocities were higher than model predictions, presumably due to the larger domain which allows higher flow velocities than predicted by the model.

The gallium concentration profile was also investigated at locations such as dendrite tips and interdendritic freckle channels. As anticipated, the fluctuations in the flow reflect the solute build-up profiles. Fig. 8a and b show the solute profiles plotted from the tip of the dendrites a–d and interdendritic channels 1–3, respectively. Solute in channel 1 exhibits significant dip near at 400 s, indicating the onset of upward natural convection. After 700 s, fluctuations in the solute profiles die down, indicating plume stabilization.

Upon observation of the solute variation in channels 1–3, the solute concentrations in all the channels simultaneously converge to an identical value at the end of stage I and prolong throughout stage II. The stabilized solute concentration was observed to gradually increase at a constant rate. This stable value of the solute in all the channels indicates the final stage of solidification where such high solute levels are typically observed and can be qualitatively compared with the experimental results reported in Ref. [18]. This also gives sufficient indication that remelting could take place, resulting in a sustained freckle channel as described in Ref. [10]. Following Ref. [45], constitutional supercooling can exist if:

$$\frac{G_L}{R} < \frac{T^{liq} - T^{sol}}{D_l}, \tag{10}$$

where G_L is the thermal gradient in the liquid, R is the solidification speed, T^{liq} and T^{sol} are liquidus and solidus temperatures for the given alloy composition, and D_l is the diffusivity of Ga in liquid In. Substituting typical values for the system under consideration, Eq. (10) is satisfied ($1.125 \times 10^8 < 5 \times 10^9$), and occurrence of remelting via constitutional supercooling can be confirmed. Furthermore, a hypothetical line can be extended backwards from the stable solute build-up as shown in Fig. 8b. During stage I, the rise in solute concentration values in the channels does not appear to exceed the extended line. This behavior suggests the presence of a threshold solute gradient which initiates natural convection and remelting during solidification.

3.4. Influence of microstructural perturbations on freckle formation

Nickel-based turbine blades can be cast as equiaxed, directionally solidified or single crystals. Several types of

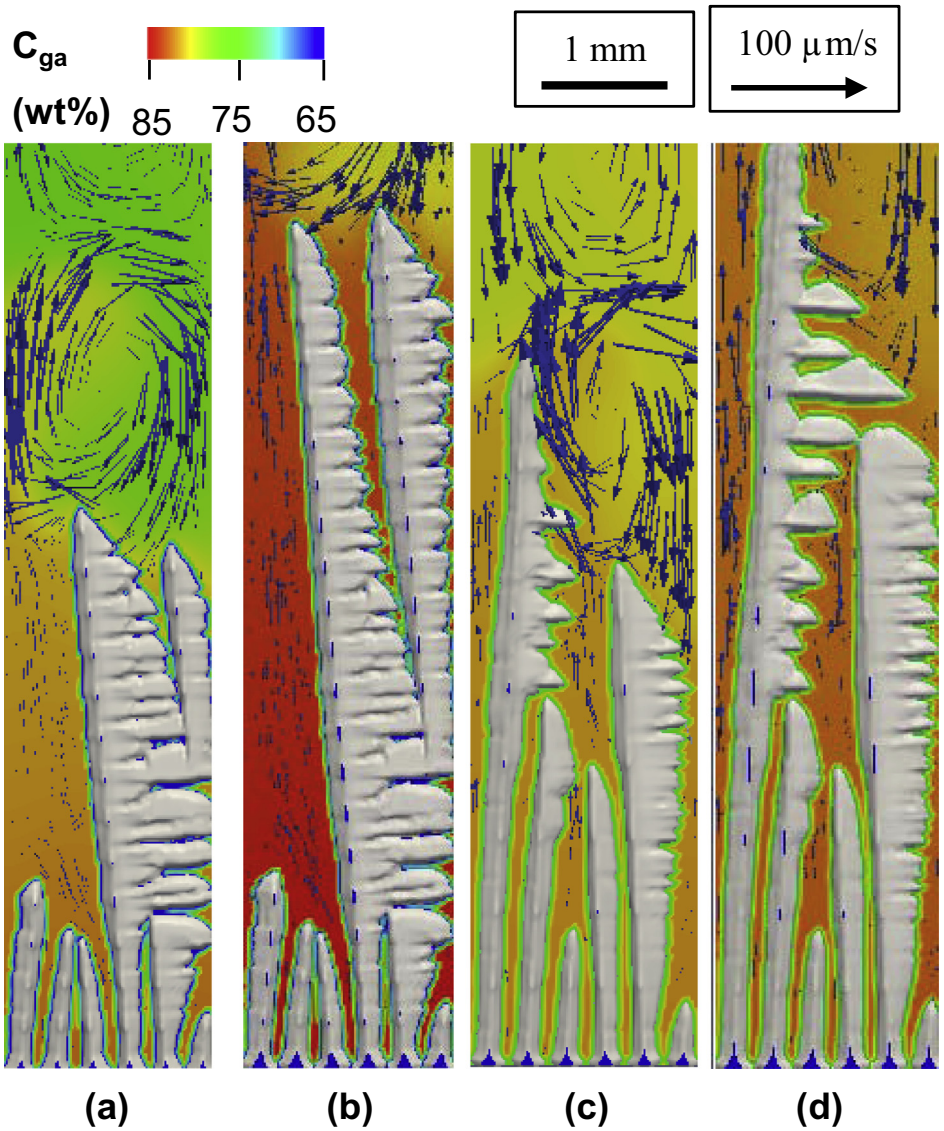

Fig. 10. Freckle formation under the influence of grain boundary defects (a, b) with $Ra = 341$ at $t =$ (a) 700 s, (b) 1400 s, and (c, d) with $Ra = 141$ at $t =$ (c) 500 s, (d) 1000 s.

Fig. 11. Freckle formation in presence of defective arm spacings (shown in black circles): (a) no defect, (b) ½λ_1, (c) λ_1/3, 2λ_1/3, (d) 2λ_1.

perturbations may occur during these casting techniques, which can eventually lead to freckles [46]. In this section, we investigate the effect of imperfections that occur in terms of grain boundary and primary arm spacing.

3.4.1. Influence of grain boundaries

Firstly, the influence of low-angle grain boundaries on freckle formation was studied. As shown schematically in Fig. 9, a set of two grains were initialized with at least

one pair of dendrites converging on to each other and another pair diverging, representing a typical low-angle grain boundary defect. By using a $7.5 \times 1.5 \times 0.15\ mm^3$ volume with a periodic boundary condition and 15 μm cells, a series of solidification conditions was simulated. Intuitively, it would seem that the diverging growth can create an extended spacing between the dendrites during solidification, thus favouring the formation of freckles. However, the simulations predicted the opposite. In a converging grain boundary defect, more solute is trapped in a gradually narrowing region, leading to localized solute enrichment. Simulations with two different solidification conditions were run, representing two distinct Rayleigh numbers: (i) $Ra = 341$ ($G = 1\ K\ mm^{-1}$, $R = 8\ \mu m\ s^{-1}$) and (ii) $Ra = 141$ ($G = 1.5\ K\ mm^{-1}$, $R = 15\ \mu m\ s^{-1}$), the latter being slightly lower than the critical value. In the first case, a plume was initiated at the converging location, and was found to gradually develop into a stable chimney (Fig. 10a and b). Although the solidification conditions are identical to those of the validation case (Section 3.1), a wider freckle channel, measuring up to 600 μm, was observed, indicating a higher propensity for defect formation. In the second case, the plume initiated from the converging location as anticipated, but did eventually stabilize from its neighboring location. The secondary arms were found to extend over the initial plume location as a result of insufficient remelting. However, the freckle channel was formed at *Ra* number lower than the critical range. The study indicates a dependence on the dendrite orientation angle (grain boundary perturbation) and a higher tendency to freckle formation. Moreover, this mainly suggested that freckles are more likely to occur in a directionally solidified casting than single-crystal blades.

3.4.2. Primary dendrite arm spacing (PDAS) variation

When casting turbine blades and other superalloy components, the PDAS often adjusts to changes in process conditions such as heat extraction, etc. This may result in localized changes in the spacing selection. In this section, we investigate the influence of variations in PDAS (λ_1) on freckle formation. Using the same conditions in Table 1, the λ_1 was both doubled ($2\ \lambda_1$) and halved ($\lambda_1/2$), and a series of simulations was performed. The majority of simulated cases demonstrate a sustained freckle channel close to the defect location when the values of *Ra* are above the critical range. The results of the simulations are shown in Fig. 11a–d) at $t = 1500$ s. The maximum gap of $2\lambda_1$ and the minimum of $\lambda_1/2$ were selected following Wang et al. [33], who demonstrated that the variation of primary arm spacing beyond these values will initiate overgrowth/undergrowth healing of the defect. From the simulations, the defective λ_1 location shows a tendency to initiate a freckle. When the spacing is narrower (less than λ), solute accumulation is enhanced in the region of irregularity (Fig. 11b). In addition, the two dendrites (third and fourth from left) undergo retarded growth due to solute-rich surroundings, and show a tendency to form the channel, but the channel is not sustained due to insufficient solute gradients. On the contrary, when the spacing is larger (greater than λ_1), the interdendritic region can accommodate larger flow rates (due to larger *Ra*), thus increasing the propensity for freckle formation (Fig. 11d). When both smaller and larger irregularities are introduced ($\lambda_1/3$ between the third and fourth grains, and $2\lambda_1/3$ between the fourth and fifth grains), a narrow but stable chimney is observed from the location where the larger spacing was imposed (Fig. 11c). Therefore, the dependence of freckle susceptibility on λ_1 can be confirmed, with a higher likelihood for spacings greater than λ_1.

4. Concluding remarks

An existing 3-D microstructural model of freckle formation was coupled with in situ X-ray radiography to investigate the mechanisms of freckle initiation and growth. The model was validated via solute concentrations, flow velocities and dendritic morphology, showing good agreement. The model was then used to gain a number of new insights.

- Key microstructural features predicted during the onset of a freckle, such as initial convection cells, were at the dendrite scale, confirming the previously proposed mechanisms.
- Two distinct stages of freckle formation were observed: initiation (with fluctuation in flow and dendrite tip velocities as recirculation cells compete), and steady growth (where one cells dominates, and flows and tip velocities stabilize). These stages are easily quantified by plotting tip velocity.
- The Ga–25 wt.% In alloy system has critical *Ra* number of 150–170.
- The freckle characteristics are found to be highly dependent on grain orientation, primary arm spacing and cooling rate. Any irregularity in these parameters strongly initiates a freckle in a close proximity to the defect.
- Converging grain boundaries were found to enhance freckle formation, a directionally solidified casting being more susceptible than single-crystal blades. In addition, a location with primary spacing greater than λ_1 was found to initiate freckles.
- The modeling approach can also be extended to perform further parametric analyses and to a range of analogous systems, including formation of freckles in steels, segregates in volcanic flows, etc.

Acknowledgements

This work was made possible by the facilities and support provided by the Manchester X-ray Imaging Facility and Research Complex at Harwell, funded in part by the EPSRC (EP/I02249X/1) and EU (RFSR-PR-10005

DDT). N.S. and S.E. gratefully acknowledge financial support from the Helmholtz alliance "LIMTECH".

Appendix A. Supplementary data

Supplementary data associated with this article can be found, in the online version, at http://dx.doi.org/10.1016/j.actamat.2014.07.002.

References

[1] Tait S, Jaupart C. Nat Publ Gr 1989;338:571.
[2] Tait S, Jahrling K, Jaupart C. Nat Publ Gr 1992;359:406.
[3] Giamei AF, Kear BH. Metall Trans 1970;1:2185.
[4] Pollock TM, Tin S. J Propuls Power 2006;22:361.
[5] Worster MG. J Fluid Mech 1992;237:649.
[6] Beckermann C. Int Mater Rev 2002;47:243.
[7] Boden S, Eckert S, Gerbeth G. Mater Lett 2010;64:1340.
[8] Guo J, Beckermann C. Numer Heat Transfer A Appl 2003;44:559.
[9] Ramirez JC, Beckermann C. Metall Mater Trans A Phys Metall Mater Sci 2003;34A:1525.
[10] Yuan L, Lee PD. Acta Mater 2012;60:4917.
[11] Reed RC, Tao T, Warnken N. Acta Mater 2009;57:5898.
[12] Madison J, Spowart J, Rowenhorst D, Aagesen LK, Thornton K, Pollock TM. Acta Mater 2010;58:2864.
[13] Beckermann C, Gu JP, Boettinger WJ. Metall Mater Trans A Phys Metall Mater Sci 2000;31:2545.
[14] Auburtin P, Wang T. Metall Mater Trans B Process Metall Mater Process Sci 2000;31:801.
[15] Pickering EJ. ISIJ Int 2013;53:935.
[16] Murakami K, Aihara H, Okamoto T. Acta Metall 1984;32:933.
[17] McDonald RJ, Hunt JD. Met Trans 1970;1:1787.
[18] Shevchenko N, Boden S, Gerbeth G, Eckert S. Metall Mater Trans A 2013;44:3797.
[19] Boden S, Eckert S, Willers B, Gerbeth G. Metall Mater Trans A 2008;39:613.
[20] Yuan L, Lee PD. Model Simul Mater Sci Eng 2010;18:055008.
[21] Yuan L, Lee PD. ISIJ Int 2010;50:1814.
[22] Felicelli SD, Heinrich JC, Poirier DR. J Cryst Growth 1998;191:879.
[23] Felicelli SD, Poirier DR, Heinrich JC. Metall Mater Trans B Process Metall Mater Process Sci 1998;29:847.
[24] Schneider MC, Beckermann C. Metall Mater Trans A 1995;26:2373.
[25] Chakraborty PR, Dutta P. J Therm Sci Eng Appl 2013;5:21004.
[26] Tan L, Zabaras N. J Comput Phys 2007;221:9.
[27] Sun ZHI, Guo M, Vleugels J, Van Der Biest O, Blanpain B. Curr Opin Solid State Mater Sci 2012;16:254.
[28] Sun DK, Zhu MF, Pan SY, Yang CR, Raabe D. Comput Math Appl 2011;61:3585.
[29] Karagadde S, Bhattacharya A, Tomar G, Dutta P. J Comput Phys 2012;231:3987.
[30] Guo Z, Mi J, Xiong S, Grant PS. Metall Mater Trans B 2013;44:924.
[31] Atwood RC, Lee PD. Acta Mater 2003;51:5447.
[32] Lee PD, Hunt JD. Acta Mater 2001;49:1383.
[33] Wang W, Lee PD, McLean M. Acta Mater 2003;51:2971.
[34] Dong HB, Lee PD. Acta Mater 2005;53:659.
[35] μMatIC Microstructural Simulation Software. <http://www3.imperial.ac.uk/engineeringalloys/research/software>.
[36] Koster JN, Derebail R. Heat Mass Transf 1997;32:489.
[37] Hunt JD, Lu SZ. Metall Mater Trans A 1996;27:611.
[38] Svirbely WJ, Selis SM. J Phys Chem 1954;58:33.
[39] Guillemot G, Gandin C-A, Bellet M. J Cryst Growth 2007;303:58.
[40] Kim B. Development of Macrosegregation During Solidifcation of Binary Metal Alloys. Pennsylvania State University; 2002.
[41] Savintsev PA, Akhkubekov AA, Getazheev KA, Rogov VI, Savvin VS. Sov Phys J 1971;14:467.
[42] Shevchenko N, Boden S, Eckert S, Borin D, Heinze M, Odenbach S. Eur Phys J Spec Top 2013;220:63.
[43] Horn BKP, Schunck BG. Artif Intell 1981;17:185.
[44] Trivedi R, Miyahara H, Mazumder P, Simsek E, Tewari SN. J Cryst Growth 2001;222:365.
[45] Kurz W, Fisher DJ. Fundamentals of Solidification. 2nd ed. Switzerland: Trans Tech Publications Ltd; 1986.
[46] Napolitano RE, Schaefer RJ. J Mater Sci 2000;35:1641.